Coherently switching the focusing characteristics of all-dielectric metalenses

FEI HE,[1,2] YU FENG,[1] HAILONG PI,[1] JIZE YAN,[1] KEVIN F. MACDONALD,[3] AND XU FANG[1,4]

[1]*School of Electronics and Computer Science, University of Southampton, SO17 1BJ, UK*
[2]*Optics and Photonics Group, University of Nottingham, NG7 2RD, UK*
[3]*Optoelectronics Research Centre and Centre for Photonic Metamaterials, University of Southampton, SO17 1BJ, UK*
[4]*x.fang@soton.ac.uk*

Abstract: Flat, gradient index, metasurface optics – in particular all-dielectric metalenses – have emerged and evolved over recent years as compact, lightweight alternative to their conventional bulk glass/crystal counterparts. Here we show that the focal properties of all-dielectric metalenses can be switched via coherent control, which is to say by changing the local electromagnetic field in the metalens plane rather than any physical or geometric property of the nanostructure or surrounding medium. The selective excitation of predominantly electric or magnetic resonant modes in the constituent cells of the metalens provides for switching, by design, of its phase profile enabling binary switching of focal length for a given lens type and, uniquely, switching between different (spherical and axicon) lens types.

1. Introduction

Coherent control has emerged in recent years as an effective and highly flexible approach for all-optical modulation – high-contrast, high-speed, low-energy switching and tuning – of electromagnetic response in planar metamaterials and ultra-thin media [1]. The technique employs two coherent, counter-propagating light beams to create a standing wave, containing a periodic pattern of electric (E) and magnetic (B) field intensity and/or polarization nodes and antinodes [2-4]. Within such standing waves, (meta)materials of substantially subwavelength thickness can be selectively exposed to different *local* excitation fields, and their response can accordingly change dramatically. The phenomenon was first demonstrated in the modulation of plasmonic metasurface absorption: at the electric field antinode (magnetic field node) of a standing wave formed by counter-propagating collinearly polarized incident beams, a suitably nanostructured thin gold film can exhibit perfect absorption, while becoming perfectly transparent at the electric field node (magnetic antinode) [3, 5]. It has subsequently been engaged to control a range of transmission, reflection, refraction, absorption and polarization phenomena, with THz bandwidth and in single- or entangled few-photon regimes [2, 3, 6-8], for applications including analogue logical data processing, pattern recognition, beam steering, and excitation-selective spectroscopy [4, 9-14].

In parallel, metalenses (i.e. metasurface-based or gradient index "flat lenses") have been established and intensively studied [15-17] as next-generation optical components with wide-ranging applications potential in imaging, microscopy, spectroscopy, lighting and display systems [18] - leveraging a compact and lightweight planar form factor and advanced lithographic nanofabrication techniques. The planar geometry also presents opportunity and advantage over conventional bulk (e.g. glass) refractive lenses in potential approaches to reversible tuning of focal properties via external stimuli: For singlet metalenses (i.e. devices that do not utilize multiple, cascaded functional layers [19-22]), mechanical and electrically-driven deformations [23-27] have been demonstrated as effective methodologies for dynamic focal tuning. Other approaches have been based on modulation of the intrinsic properties of constituent or surrounding media, including liquid crystals thermo-optic polymers, chalcogenides, and 2D materials [28-40].

Establishing coherent control as a new tuning strategy for metalenses may combine the best of both technologies. Most noticeably, Ref [10] achieved dynamic focal tuning on a plasmonic metasurface. Because the plasmonic metasurface functions as an ultrathin beam-splitter, the tuning requires the incident light to be structured, as opposed to plane waves that are adopted in a typical coherent control configuration. In this work, we establish design principles for coherently controlled focal characteristic switching in all-dielectric metalenses. As examples, we introduce and computationally analyze designs for silicon spherical and axicon lenses with coherently-controlled focal lengths and Bessel-beam widths/depths that change by up to a factor of 2 in the transition between local E and B field antinode illumination regimes, and a lens that can be switched between spherical and axicon configurations.

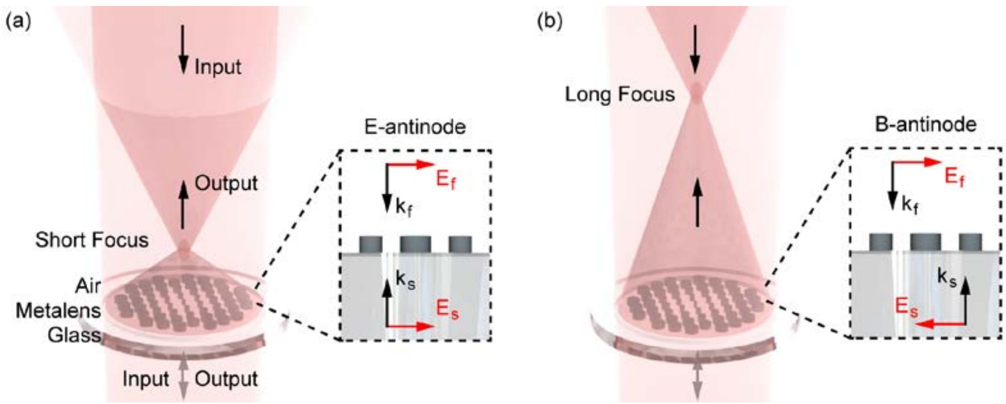

Fig. 1. Coherent switching of metalens focus. The metalens, comprised of an array of Si nanopillars on a glass substrate, is illuminated by counter-propagating coherent light beams at normal incidence, one from free-space (with electric field and wave vector E_f and k_f, respectively) and the other through the substrate (E_s and k_s). Changing the relative phase and amplitude of E_f and E_s can position the metalens at either (a) the electric antinode [E-antinode] or (b) the magnetic antinode [B-antinode] of the standing wave formed by the two input beams. The focusing properties of the metalens, manifested in the output beams, change accordingly.

We consider metalenses comprising arrays of elliptical Si nanopillars on a semi-infinite glass substrate, illuminated by two coherent, counter-propagating, collinearly polarized light beams at normal incidence – one from the substrate side with incident electric field E_s, and one from free space with field E_f. The surface of the substrate can be selectively located at an E-antinode [Fig. 1(a)] or a B-antinode [Fig. 1(b)] of a standing wave, depending upon the relative phase and amplitude of the two incident fields [4]: The E-antinode condition is achieved when E_f and E_s are parallel and of equal magnitude ($E_f/E_s = 1$) at the surface [Fig. 1(a), inset]; while the B-antinode condition requires E_f and E_s to be anti-parallel with relative amplitudes dependent upon the ratio of incident media refractive indices ($E_f/E_s = -n_s/n_f$) [Fig. 1(b), inset]. Silicon is employed for the nanopillar resonators, as a high-refractive index, low optical absorption dielectric for the near-infrared wavelengths of interest, with established capacity to support Mie-type resonances with scattered field phase shifts covering the necessary 2π range, in structures with readily achievable dimensions [41, 42].

2. Phase of light scattered by individual nanopillars

To enable the development of coherently controllable metalens designs, we first evaluate the scattering characteristics of individual nanopillars as a function of size under regimes of E- and B-antinode illumination (Fig. 2) at a free-space wavelength of 1550 nm, with the light polarization along the x direction in all cases. Simulations are performed using a full-wave finite element electromagnetic solver (COMSOL Multiphysics) using purely real refractive index values for silicon and glass of 3.48 and 1.50, respectively. We assume a fixed pillar height (z) of 500 nm and elliptical xy plane cross sections with principal semi-axis dimensions R_x and R_y each ranging from 100 to 400 nm in 5 nm steps – a library of 61 × 61 = 3721 nanopillar geometries. The simulations employ periodic boundary conditions in the xy plane, with a 900 nm center-to-center spacing between pillars that is smaller than the wavelength (to exclude diffraction) but large enough to negate coupling among neighboring pillars [43], i.e. such that the collective scattering characteristics can be taken as those of singular pillars.

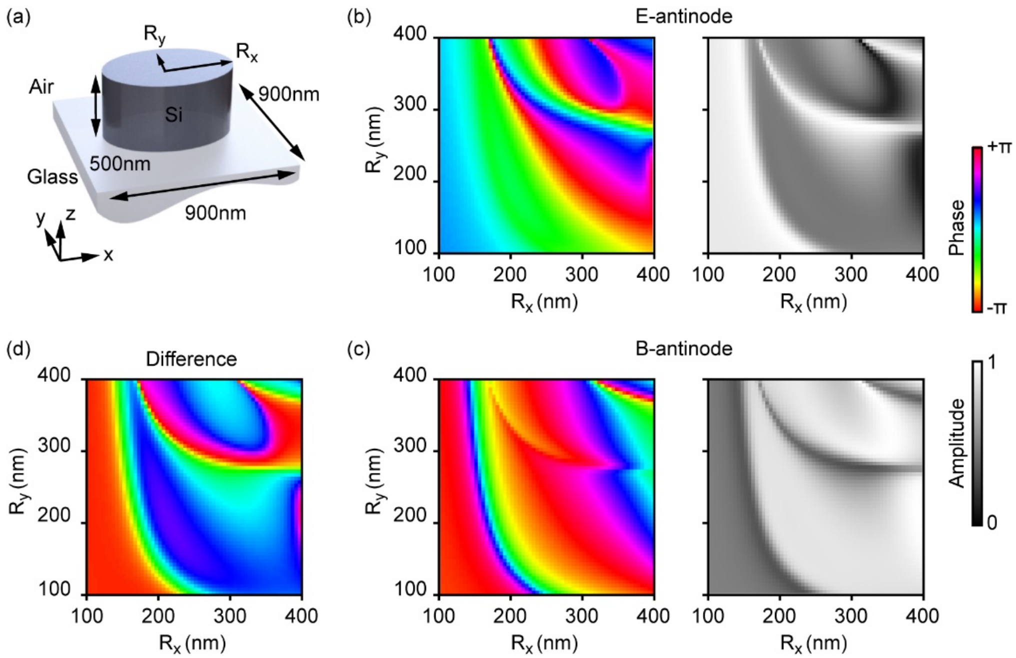

Fig. 2. Nanopillar scattering phase. (a) Dimensional schematic of a single Si nanopillar unit cell. Elliptical pillars with semi-axial dimensions R_x and R_y are centered within each 900 nm × 900 nm unit cell in an infinitely large, bi-periodic array. (b, c) Scattering phase and amplitude as functions of R_x and R_y [values ranging from 100 to 400 nm in 5 nm steps; x-polarized incident light] for (b) E-antinode and (c) B-antinode coherent illumination conditions. (d) Phase difference between (c) and (d). All the phase values are relative to that of the free-space incident beam, which remains unchanged between the two illumination conditions.

Figures 2(b) and 2(c) show the phase and amplitude of scattered light as a function of R_x and R_y for the two (E- and B-antinode) illumination regimes. The first thing to note is that in both cases, the selected range of pillar dimensions provides full coverage of a 2π range. This can represent a challenge in the design of any gradient metasurface optical elements [44, 45] but under standing wave illumination conditions, one can selectively excite electric or magnetic type modes while almost entirely suppressing the other, thereby gaining access to a wider range of scattering phases for a given set of pillar dimensions than is possible under single beam illumination. (The finite, nonzero height of the pillars precludes total suppression of any magnetic, B, contribution under the E-antinode illumination regime, and vice versa.) The second, which is of fundamental importance to coherent modulation of metalens functionality, is the difference between Figs. 2(b) and 2(c) [Fig. 2(d)] – i.e. the fact that under E/B-antinode standing wave illumination a given nanopillar offers two (generally) different values of scattering phase, as compared to a single value under single beam illumination.

3. Design process for coherently switchable metalenses

Metalenses are subsequently designed as square arrays of nanopillars with center-to-center spacing of 900 nm, filling a circular area of radius 36 μm – a total of 4777 lattice sites, each occupied by a pillar selected from the above library to provide the best possible simultaneous fit to the two (different) radial phase gradient profiles required for the lens to focus light (differently) under both E- and B-antinode illumination conditions. The semi-axes (R_x and R_y) of the pillars are oriented along the translation directions of the metalens lattice sites [the *x* and *y* axes respectively, with coordinates defined relative to the center of the metalens, as illustrated in Fig. 3(a)].

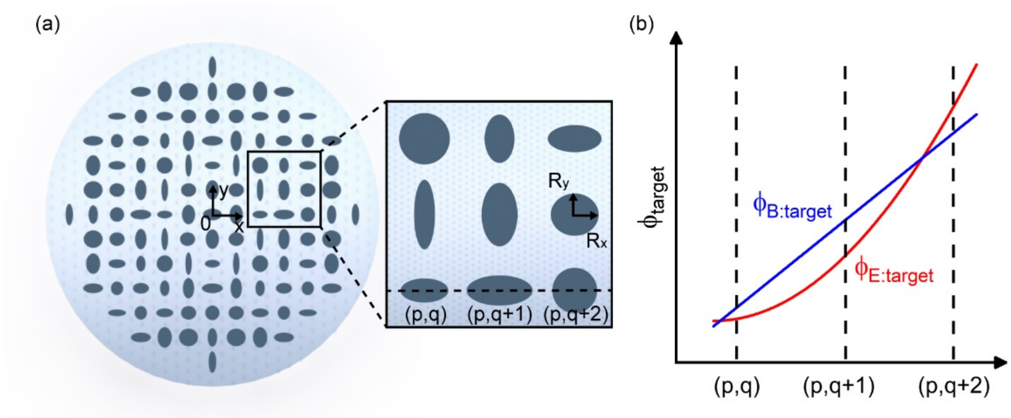

Fig. 3. Metalens design principle. (a) Lenses are assembled as a square lattice of cells with center-to-center spacing of 900 nm, filling a circular area of radius 36 μm [far fewer cells being shown in this schematic]. Each cell contains an elliptical Si nanopillar from the library of Fig. 2, with semi-axes (R_x and R_y) aligned to the *x*, *y* coordinate frame of the array. (b) The nanopillar at each location, with coordinates (*p*, *q*), is selected to fit a pair of target phase profiles $\phi_{E:target}$ and $\phi_{B:target}$ for E- and B-antinode illumination conditions, respectively.

Optimal nanopillar dimensions (R_x and R_y) are identified for each lattice site by minimizing a summation over the lens of the following quantity, evaluated at each lattice site – the combined deviation from the ideal pair of scattered phase values at that point:

$$\left|\phi_E^{p,q} - \phi_{E:target}^{p,q} - \phi_{E:base} - n^{p,q}2\pi\right| + \left|\phi_B^{p,q} - \phi_{B:target}^{p,q} - \phi_{B:base} - m^{p,q}2\pi\right| \quad (1)$$

Here, $\phi_E^{p,q}$ and $\phi_B^{p,q}$ are the two antinodal scattered phase values of the nanopillar geometry under consideration [i.e. from matching R_x and R_y coordinates in Figs. 2(b) and 2(c)], and $\phi_{E:target}^{p,q}$ and $\phi_{B:target}^{p,q}$ are the corresponding target phase values for the lattice point; *p* and *q* being the positional coordinates of the lattice point. $\phi_{E:base}$ and $\phi_{B:base}$ are arbitrary offsets, which can independently take values between -π and +π (in steps of π/500 for the purposes of the numerical optimization procedure) but must be constant across the whole lens (adding or subtracting a constant phase at all points has no net effect on the collective phase profile). They account for the fact that it is only necessary to constrain relative phase as a function of lattice coordinate relative to the center of the lens, rather than absolute phase. *n* and *m* are arbitrary (independent) integers, which account for equivalence of ±π values (and multiples thereof). As a final step, the focusing performance of the full metalens design is evaluated using a finite difference time domain numerical solver (Lumerical FDTD Solutions; with incident light polarized along *x* as in singular pillar library simulations above) - this being more computationally efficient for large assemblies of non-identical unit cells than the finite element method employed above in generating the nanopillar library.

4. Coherently switchable metalens functionalities

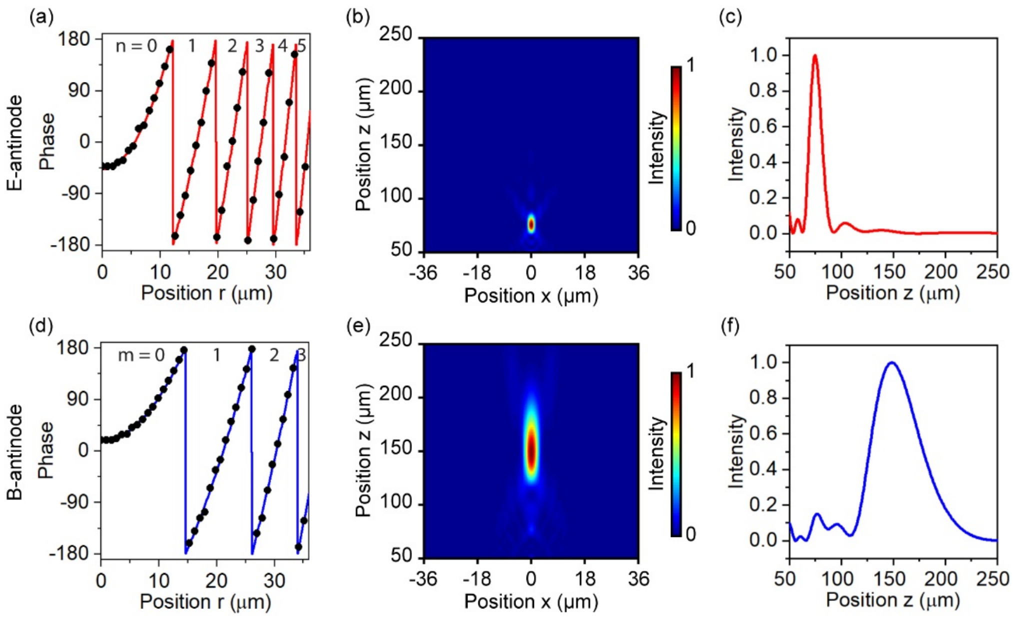

Fig. 4. Coherent switching of a spherical metalens. (a and d) Target phase profiles (lines) for (a) E-antinode and (d) B-antinode illumination, as functions of radial distance from the center of the metalens, overlaid with points corresponding to the co-optimally selected Si nanopillars along the *x* axis of the lens. (b and e) Corresponding output electric field intensities - i.e. of light propagating in the +z direction away from the lens - in the *xz* plane from 50 to 250 μm above the metalens surface. The intensity is normalized against the maximal value in the map. (c and f) Intensity as a function of distance from the metalens surface along the output beam axes [the lines *x* = 0 in panels (b) and (e)].

We first consider metalenses that produce a spherical wavefront in free space. These require a hyperbolic phase profile:

$$\phi(f,r) = 2\pi(\sqrt{r^2+f^2} - f)/\lambda \tag{2}$$

where λ is the free space wavelength of 1550 nm, *r* is radial distance from the center of the lens, and *f* is the focal length. We select values of *f* differing by a factor of two: 75 μm at the E-antinode and 150 μm the B-antinode. Figures 4(a) and 4(d) show the corresponding $\phi_{E:target}$ and $\phi_{B:target}$ radial phase profiles as solid lines, overlaid with points relating to the set of forty nanopillars that provides a best fit to both [according to Eq.(1)] along the y = 0 direction. Optimal $\phi_{E:base}$ and $\phi_{B:base}$ values for this lens are found to be -47.2° and 16.6°. The nanopillar library defined above enables equally good phase matching to the required profiles over the entire lens area, with average phase deviation from ideal values of 3.1° at the E-antinode and 2.6° at the B-antinode, over all 4777 lattice points. In consequence, the lens generates well-defined, singular foci under both E- and B-antinode illumination conditions [Figs. 4(b, c) and 4(e, f)]: at the E-antinode, *f* = 74.7 μm (vs. a target value of 75.0 μm), the full-width half-maximum (FWHM) spot diameter is 1.2λ, and the FWHM focal depth is 8.5λ; at the B-antinode, *f* = 148.3 μm (vs. a target value of 150 μm), the FWHM spot diameter is 2.4λ, and the FWHM focal depth is 33.7λ. The focusing efficiency, defined as the power ratio of the focal spot and the total input, is 12.9% at the E-antinode and 31.1% at the B-antinode.

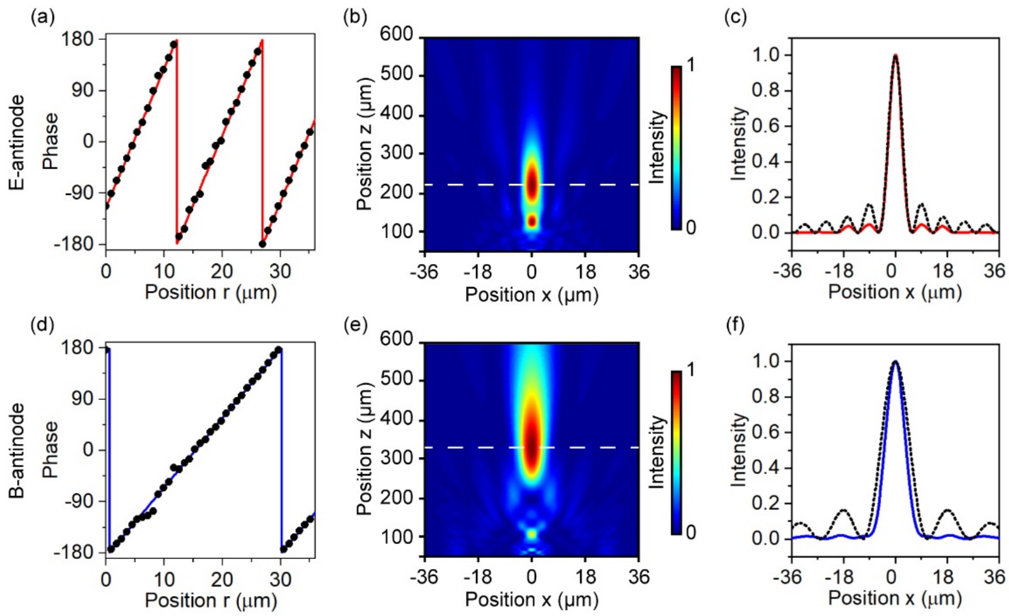

Fig. 5. Coherent switching of an axicon metalens. (a and d) Target phase profiles (lines) for (a) E-antinode and (d) B-antinode illumination, as functions of radial distance from the center of the metalens, overlaid with points corresponding to the co-optimally selected Si nanopillars along the *x* axis of the lens. (b and e) Corresponding output electric field intensities in the *xz* plane from 50 to 600 μm above the metalens surface. (c and f) Cross sectional intensity profiles (solid lines) of the output field at (c) $z = 219.0$ μm in panel (b), and (f) $z = 331.9$ μm in panel (e) [as indicated by the dashed white lines in said panels] overlaid with zeroth-order Bessel functions of the first kind (black dotted lines).

As a second example (Fig. 5), we consider a coherently switchable axicon metalens with a conical phase profile $\phi(f, r)$:

$$\phi(f, r) = 2\pi\, r\, sin\beta/\lambda \tag{3}$$

where the coefficient β dictates the slope of the phase profile. The Bessel-like beams generated by axicons possess unique properties in that they are non-diffracting (e.g. capable of maintaining its transversal intensity profile in propagation) and self-healing (e.g. capable of recovering its original beam profile even if it is obstructed by a finite sized object), which are of value in applications such as optical coherence tomography, particle manipulation and cell sorting [11, 46-49]. We select values of β differing by a factor of two: 6° at the E-antinode and 3° the B-antinode. As per Fig. 4 for the spherical lens, Figs 5(a) and 5(d) show the corresponding $\phi_{E:target}$ and $\phi_{B:target}$ radial phase profiles as solid lines, overlaid with points relating to the set of forty nanopillars that provides a best fit to both [according to Eq.(1)] along the y = 0 direction. Optimal $\phi_{E:base}$ and $\phi_{B:base}$ values for this lens are -114.1° and 173.5°. Again, good phase matching is achieved over the whole lens area, with average phase deviation of 2.6° at the E-antinode and 2.2° at the B-antinode. Figures 5(b, c) and 5(e, f) illustrate focusing performance: at the E-antinode, the axial focus has a FWHM diameter of 3.3λ, and a FWHM focal depth of 84.8λ; at the B-antinode, it has a FWHM diameter of 5.0λ, and a FWHM focal depth of 173.8λ. The focusing efficiency is 13.0% at the E-antinode and 29.0% at the B-antinode. Compared to the foci of the spherical metalens above [Figs. 4(b) and 4(e)], the axicon foci [Figs. 5(b) and 5(e)] are extended in the *z* direction and have pronounced sidebands, which are key characteristics of Bessel beams generated by axicons [46]. The cross-sectional intensity distribution in the focal plane is well-matched to that of an ideal Bessel beam with minor deviations [Figs. 5(c) and 5(f)], indicative of a clear slope-angle change between the conical phase profiles at E- and B-antinodes. These discrepancies, and the appearance of secondary axial focal points, are attributed to the limited aperture size of the metalens, imperfect phase matching, and variations in light scattering strength among the nanopillars [50].

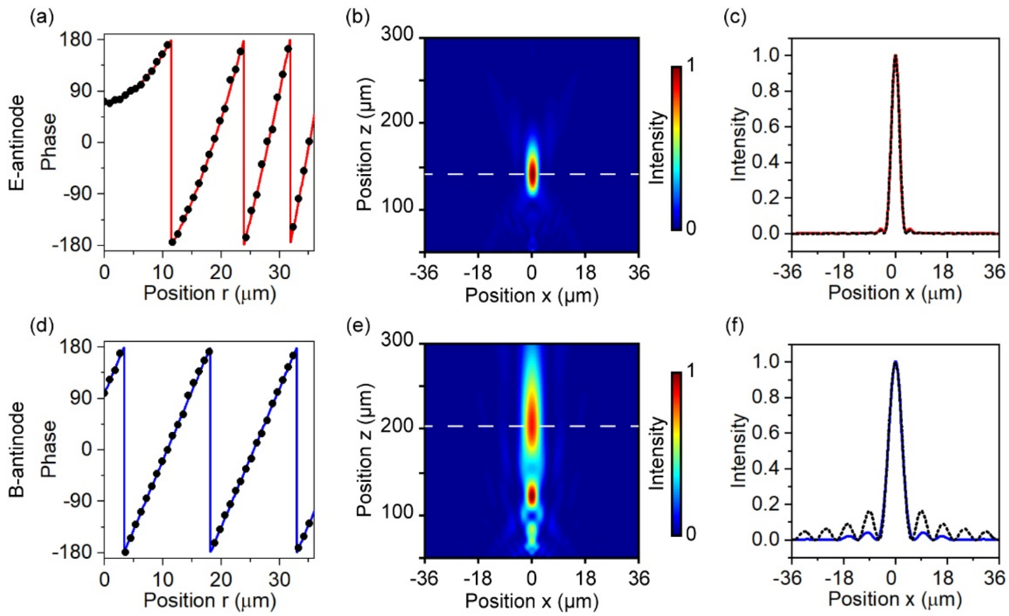

Fig. 6. Coherent switching between (a-c) a spherical lens and (d-f) an axicon lens. (a and d) Target phase profiles (lines) for (a) a spherical lens under E-antinode illumination and (d) an axicon lens under B-antinode illumination, as functions of radial distance from the center of the metalens, overlaid with points corresponding to the co-optimally selected Si nanopillars along the x axis of the lens. (b and e) Corresponding output electric field intensities in the xz plane from 50 to 250 μm above the metalens surface. (c and f) Cross sectional intensity profiles (solid lines) of the output field at (c) 139.5 μm in panel (b) overlaid with the analytical profile of an Airy pattern (black dashed line), and (f) z = 204.7 μm in panel (e) overlaid with zeroth-order Bessel functions of the first kind (black dotted lines).

The two examples above illustrate coherent switching of focal parameters for lenses of fixed type (spherical or axicon) but the coherent control paradigm also allows for switching between lens types – a functionality that cannot be straightforwardly implemented by other tuning mechanisms, such as mechanical deformation or homogenous change of intrinsic material properties [23, 24, 26-39]. In the third example here (Fig. 6), we design a metalens with hyperbolic profile [Eq. (2)] at the E-antinode – to function as a spherical lens with f = 140 µm, and a conical profile [Eq. (3)] at the B-antinode – an axicon with β = 6°. The range of achievable phase modulation (Fig. 2) facilitates excellent phase matching through this hyperbolic-conical profile transition, with average phase deviation of 3.0° at the E-antinode and 2.5° at B-antinode. Figures 6(b, c) and 6(e, f) illustrate that, at the E-antinode, f = 139.5 µm (vs. a target value of 140 μm) with a FWHM spot diameter of 2.1λ and a FWHM field depth of 29.0λ; at the B-antinode, the main section of the focal field has a FWHM diameter of 3.4λ and a FWHM depth of 67.3λ. Once more, the significant difference in focal depth [Figs. 6(b, e)] and side band [Figs. 6(c, f)] at E- and B-antinodes prove a pronounced transition between parabolic and axicon lenses, indicating that the coherent control method is a promising approach for flexible wavefront shaping.

5. Conclusion

In summary, we introduce coherent control/illumination as a versatile approach to realizing binary focal switching in all-dielectric metalenses. The constituent Si nanopillars of the metalenses respond to local driving field, and under standing wave illumination the selective excitation of their electric or magnetic resonant modes can provide, by design, markedly different metalens phase profiles. Lenses are designed as arrays of nanopillars with elliptical cross-sectional dimensions individually selected to co-optimally fit the desired pair of phase profiles. In proof of principle here, we analyze designs for near-IR spherical and axicon lenses with switchable focal lengths and diameters differing by a factor of two, and a lens that can be switched between spherical and axicon forms. The concept though is not limited to these two lens types and, with appropriate selection of resonator material and geometry, can be adapted to other spectral bands to enable reversible, all-optical control of output wavefronts.

As in any other interferometric phenomenon or device, for a high contrast between the limiting (constructive/destructive, or in this case E/B-antinode) states, coherently controlled metalenses require accurate beam alignment/stability and wavefront uniformity over the lens area. And like any other optically resonant metasurface element, the lenses considered here – designed to function at one specific wavelength – would be subject to chromatic aberration. However, approaches to the design of achromatic metalenses are well known [16, 17, 50] and the spectral dispersion of scattering can be taken into account (as required according to application) in nanopillar selection at the lens design stage. Likewise, manufacturing tolerances and systematic imperfections can be accounted for in designs by compiling the E/B-antinode nanopillar libraries on the basis of real (i.e. measured) pillar geometries including, for example, rounded corners and tapered side walls. And finally, where output efficiency is of primary concern, greater weight can be given to scattering amplitudes in the selection of nanopillars for optimum lens performance. As such, the dual libraries-based selection offers a highly flexible and adaptable approach to application-specific lens design.

Funding. Engineering and Physical Sciences Research Council (EP/M009122/1); Royal Society (IEC\R3\183071, IES\R3\183086).

Disclosures. The authors declare no conflicts of interest.

Data availability. The data that support the findings of this study are available within the article.

References

1. E. Plum, K. F. MacDonald, X. Fang, D. Faccio, and N. I. Zheludev, "Controlling the Optical Response of 2D Matter in Standing Waves," ACS Photonics **4**, 3000-3011 (2017).
2. X. Fang, K. F. MacDonald, E. Plum, and N. I. Zheludev, "Coherent control of light-matter interactions in polarization standing waves," Sci Rep **6**, 31141 (2016).
3. J. F. Zhang, K. F. MacDonald, and N. I. Zheludev, "Controlling light-with-light without nonlinearity," Light-Sci Appl **1**, e18 (2012).
4. F. He, K. F. MacDonald, and X. Fang, "Coherent illumination spectroscopy of nanostructures and thin films on thick substrates," Opt Express **26**, 12415-12423 (2018).
5. D. G. Baranov, A. Krasnok, T. Shegai, A. Alu, and Y. D. Chong, "Coherent perfect absorbers: linear control of light with light," Nat Rev Mater **2**, 17064 (2017).
6. X. Fang, K. F. MacDonald, and N. I. Zheludev, "Controlling light with light using coherent metadevices: all-optical transistor, summator and invertor," Light-Sci Appl **4**, e292 (2015).
7. A. Xomalis, I. Demirtzioglou, E. Plum, Y. M. Jung, V. Nalla, C. Lacava, K. F. MacDonald, P. Petropoulos, D. J. Richardson, and N. I. Zheludev, "Fibre-optic metadevice for all-optical signal modulation based on coherent absorption," Nat Commun **9**, 182 (2018).
8. A. Espinosa-Soria, E. Pinilla-Cienfuegos, F. J. Diaz-Fernandez, A. Griol, J. Marti, and A. Martinez, "Coherent Control of a Plasmonic Nanoantenna Integrated on a Silicon Chip," ACS Photonics **5**, 2712-2717 (2018).
9. M. Papaioannou, E. Plum, and N. I. Zheludev, "All-Optical Pattern Recognition and Image Processing on a Metamaterial Beam Splitter," ACS Photonics **4**, 217-222 (2017).
10. M. Papaioannou, E. Plum, E. T. F. Rogers, and N. I. Zheludev, "All-optical dynamic focusing of light via coherent absorption in a plasmonic metasurface," Light-Sci Appl **7**, e17157 (2018).
11. S. Q. Yin, F. He, W. Kubo, Q. Wang, J. Frame, N. G. Green, and X. Fang, "Coherently tunable metalens tweezers for optofluidic particle routing," Opt Express **28**, 38949-38959 (2020).
12. Z. Y. Zhang, M. Kang, X. Q. Zhang, X. Feng, Y. H. Xu, X. Y. Chen, H. F. Zhang, Q. Xu, Z. Tian, W. L. Zhang, A. Krasnok, J. G. Han, and A. Alu, "Coherent Perfect Diffraction in Metagratings," Adv Mater **32**, 2002341 (2020).
13. F. He, K. F. MacDonald, and X. Fang, "Continuous beam steering by coherent light-by-light control of dielectric metasurface phase gradient," Opt Express **28**, 30107-30116 (2020).

14. J. Shi, X. Fang, E. T. F. Rogers, E. Plum, K. F. MacDonald, and N. I. Zheludev, "Coherent control of Snell's law at metasurfaces," Opt Express **22**, 21051-21060 (2018).
15. R. Paniagua-Dominguez, Y. F. Yu, E. Khaidarov, S. M. Choi, V. Leong, R. M. Bakker, X. N. Liang, Y. H. Fu, V. Valuckas, L. A. Krivitsky, and A. I. Kuznetsov, "A Metalens with a Near-Unity Numerical Aperture," Nano Lett **18**, 2124-2132 (2018).
16. W. T. Chen, A. Y. Zhu, V. Sanjeev, M. Khorasaninejad, Z. J. Shi, E. Lee, and F. Capasso, "A broadband achromatic metalens for focusing and imaging in the visible," Nat Nanotechnol **13**, 220-226 (2018).
17. R. J. Lin, V. C. Su, S. M. Wang, M. K. Chen, T. L. Chung, Y. H. Chen, H. Y. Kuo, J. W. Chen, J. Chen, Y. T. Huang, J. H. Wang, C. H. Chu, P. C. Wu, T. Li, Z. L. Wang, S. N. Zhu, and D. P. Tsai, "Achromatic metalens array for full-colour light-field imaging," Nat Nanotechnol **14**, 227-231 (2019).
18. G. Y. Lee, J. Y. Hong, S. Hwang, S. Moon, H. Kang, S. Jeon, H. Kim, J. H. Jeong, and B. Lee, "Metasurface eyepiece for augmented reality," Nat Commun **9**, 4562 (2018).
19. N. Yilmaz, A. Ozdemir, A. Ozer, and H. Kurt, "Rotationally tunable polarization-insensitive single and multifocal metasurface," J Opt **21**, 045105 (2019).
20. F. Balli, M. A. Sultan, and J. T. Hastings, "Rotationally tunable varifocal 3D metalens," Opt Lett **46**, 3548-3551 (2021).
21. X. Che, R. Gao, Y. Yu, W. Liu, Y. Sun, D. Zhu, W. Qiao, L. Wang, J. Zhang, Q. Yuan, and Z. Gao, "Generalized phase profile design method for tunable devices using bilayer metasurfaces," Opt Express **29**, 44214-44226 (2021).
22. Y. Chen, S. Pu, C. Wang, and F. Yi, "Voltage tunable mid-wave infrared reflective varifocal metalens via an optomechanic cavity," Opt Lett **46**, 1930-1933 (2021).
23. H. S. Ee and R. Agarwal, "Tunable Metasurface and Flat Optical Zoom Lens on a Stretchable Substrate," Nano Lett **16**, 2818-2823 (2016).
24. S. M. Kamali, E. Arbabi, A. Arbabi, Y. Horie, and A. Faraon, "Highly tunable elastic dielectric metasurface lenses," Laser Photonics Rev **10**, 1002-1008 (2016).
25. A. She, S. Y. Zhang, S. Shian, D. R. Clarke, and F. Capasso, "Adaptive metalenses with simultaneous electrical control of focal length, astigmatism, and shift," Sci Adv **4**, eaap9957 (2018).
26. C. H. Liu, J. J. Zheng, S. Colburn, T. K. Fryett, Y. Y. Chen, X. D. Xu, and A. Majumdar, "Ultrathin van der Waals Metalenses," Nano Lett **18**, 6961-6966 (2018).
27. F. Cheng, L. Y. Qiu, D. Nikolov, A. Bauer, J. P. Rolland, and A. N. Vamivakas, "Mechanically tunable focusing metamirror in the visible," Opt Express **27**, 15194-15204 (2019).
28. C. Y. Fan, T. J. Chuang, K. H. Wu, and G. D. J. Su, "Electrically modulated varifocal metalens combined with twisted nematic liquid crystals," Opt Express **28**, 10609-10617 (2020).
29. Z. Shen, S. Zhou, X. Li, S. Ge, P. Chen, W. Hu, and Y. Lu, "Liquid crystal integrated metalens with tunable chromatic aberration," Advanced Photonics **2**, 036002 (2020).
30. A. Afridi, J. Canet-Ferrer, L. Philippet, J. Osmond, P. Berto, and R. Quidant, "Electrically Driven Varifocal Silicon Metalens," ACS Photonics **5**, 4497-4503 (2018).
31. X. H. Yin, T. Steinle, L. L. Huang, T. Taubner, M. Wuttig, T. Zentgraf, and H. Giessen, "Beam switching and bifocal zoom lensing using active plasmonic metasurfaces," Light-Sci Appl **6**, e17016 (2017).
32. W. Bai, P. Yang, J. Huang, D. B. Chen, J. J. Zhang, Z. J. Zhang, J. B. Yang, and B. Xu, "Near-infrared tunable metalens based on phase change material $Ge_2Se_2Te_5$," Sci Rep **9**, 5368 (2019).
33. M. Y. Shalaginov, S. An, Y. F. Zhang, F. Yang, P. Su, V. Liberman, J. B. Chou, C. M. Roberts, M. Kang, C. Rios, Q. Y. Du, C. Fowler, A. Agarwal, K. A. Richardson, C. Rivero-Baleine, H. L. Zhang, J. J. Hu, and T. Gu, "Reconfigurable all-dielectric metalens with diffraction-limited performance," Nat Commun **12**, 1225 (2021).
34. P. Yu, J. X. Li, S. Zhang, Z. W. Jin, G. Schutz, C. W. Qiu, M. Hirscher, and N. Liu, "Dynamic Janus Metasurfaces in the Visible Spectral Region," Nano Lett **18**, 4584-4589 (2018).
35. P. P. Iyer, R. A. DeCrescent, T. Lewi, N. Antonellis, and J. A. Schuller, "Uniform Thermo-Optic Tunability of Dielectric Metalenses," Phys Rev Appl **10**, 044029 (2018).
36. Z. D. Huang, B. Hu, W. G. Liu, J. Liu, and Y. T. Wang, "Dynamical tuning of terahertz meta-lens assisted by graphene," J Opt Soc Am B **34**, 1848-1854 (2017).
37. W. G. Liu, B. Hu, Z. D. Huang, H. Y. Guan, H. T. Li, X. K. Wang, Y. Zhang, H. X. Yin, X. L. Xiong, J. Liu, and Y. T. Wang, "Graphene-enabled electrically controlled terahertz meta-lens," Photonics Res **6**, 703-708 (2018).
38. H. X. Zhou, J. R. Cheng, F. Fan, X. H. Wang, and S. J. Chang, "Graphene-based transmissive terahertz metalens with dynamic and fixed focusing," J Phys D Appl Phys **53**, 025105 (2020).
39. Z. K. Zhang, X. Q. Qi, J. F. Zhang, C. C. Guo, and Z. H. Zhu, "Graphene-enabled electrically tunability of metalens in the terahertz range," Opt Express **28**, 28101-28112 (2020).
40. J. van de Groep, J. H. Song, U. Celano, Q. T. Li, P. G. Kik, and M. L. Brongersma, "Exciton resonance tuning of an atomically thin lens," Nat Photonics **14**, 426-430 (2020).
41. M. Decker, I. Staude, M. Falkner, J. Dominguez, D. N. Neshev, I. Brener, T. Pertsch, and Y. S. Kivshar, "High-Efficiency Dielectric Huygens' Surfaces," Adv Opt Mater **3**, 813-820 (2015).
42. Y. F. Yu, A. Y. Zhu, R. Paniagua-Dominguez, Y. H. Fu, B. Luk'yanchuk, and A. I. Kuznetsov, "High-transmission dielectric metasurface with 2π phase control at visible wavelengths," Laser Photonics Rev **9**, 412-418 (2015).

43. S. M. Kamali, E. Arbabi, A. Arbabi, and A. Faraon, "A review of dielectric optical metasurfaces for wavefront control," Nanophotonics **7**, 1041-1068 (2018).
44. W. W. Wan, J. Gao, and X. D. Yang, "Full-Color Plasmonic Metasurface Holograms," ACS Nano **10**, 10671-10680 (2016).
45. Y. J. Bao, J. C. Ni, and C. W. Qiu, "A Minimalist Single-Layer Metasurface for Arbitrary and Full Control of Vector Vortex Beams," Adv Mater **32**, 1905659 (2020).
46. M. Mazilu, D. J. Stevenson, F. Gunn-Moore, and K. Dholakia, "Light beats the spread: "non-diffracting" beams," Laser Photonics Rev **4**, 529-547 (2010).
47. F. Aieta, P. Genevet, M. A. Kats, N. F. Yu, R. Blanchard, Z. Gahurro, and F. Capasso, "Aberration-Free Ultrathin Flat Lenses and Axicons at Telecom Wavelengths Based on Plasmonic Metasurfaces," Nano Lett **12**, 4932-4936 (2012).
48. D. M. Lin, P. Y. Fan, E. Hasman, and M. L. Brongersma, "Dielectric gradient metasurface optical elements," Science **345**, 298-302 (2014).
49. W. T. Chen, M. Khorasaninejad, A. Y. Zhu, J. Oh, R. C. Devlin, A. Zaidi, and F. Capasso, "Generation of wavelength-independent subwavelength Bessel beams using metasurfaces," Light-Sci Appl **6**, e16259 (2017).
50. M. Khorasaninejad, Z. Shi, A. Y. Zhu, W. T. Chen, V. Sanjeev, A. Zaidi, and F. Capasso, "Achromatic Metalens over 60 nm Bandwidth in the Visible and Metalens with Reverse Chromatic Dispersion," Nano Lett **17**, 1819-1824 (2017).